scientific reports

Check for updates

OPEN

Study on the disaster mechanism and prevention technology of embankment slip-collapse after extreme rainfall in the loess area

Jiawei Fan[1,2], Yufang Zhang[1,2], Yang Peng[1,2], Zheyuan Xing[1,2], Kun Yuan[1,2], Jian Cui[1,2], Bo Liu[1,2] & Wenjiao Zhou[1,2]✉

This study investigates railway embankment slip-collapse disasters triggered by July 2021 extreme rainfall in Zhengzhou, China, through field investigations, in-situ tests, laboratory tests, field monitoring, and numerical simulations. The research results indicate that: (1) Zhengzhou loess experiences accelerated strength degradation when moisture content exceeds plastic limit, with shear modulus, cohesion, and internal friction angle decreasing rapidly beyond this threshold. (2) Embankment slip-collapse, a geohazard characterized by shallow failures in slope surfaces, is primarily triggered by hydro-mechanical coupling under extreme rainfall, with deformation severity controlled by infiltration intensity. (3) Three stages of slope stability division criteria are proposed, namely metastable zone, critical instability zone, and instability zone. The critical threshold of moisture content of 20.71% under these conditions provides a quantifiable benchmark for early warning systems targeting surface collapse prevention. (4) A steel grouting pipe reinforcement technique demonstrated effective stabilization, achieving 251 kN anchoring force and improved stratum integrity. Surface wave tests, numerical simulations, and field monitoring confirmed significant displacement control and enhanced slope stability under extreme rainfall conditions. The research results provide critical insights for transportation infrastructure protection against extreme rainfall conditions.

Keywords Slope engineering, Extreme rainfall, Loess, Slip-collapse, Disaster mechanism, Prevention technology

In July 2021, Henan Province, China, experienced extreme rainfall. 147.86 million people in 150 counties suffered from the severe disaster. The direct economic losses amounted to 120.06 billion yuan. Railway facilities suffered severe damage, especially in the Zhengzhou area where railway embankments were eroded by heavy rainfall, leading to numerous embankment slope disasters. Among them, embankment slip-collapse disasters were the most typical, accounting for over 60% of the total embankment slope disasters. Therefore, in-depth study of the disaster mechanism and prevention techniques of such disasters caused by extreme rainfall has practical value for prevention and control efforts.

Over the years, many scholars have conducted research on water damaged disasters' issues in various geological engineering projects[1–13]. Research on water damage to embankment slopes primarily focuses on theoretical studies and practical results. In terms of theoretical research, scholars have mainly concentrated on theoretical innovations in the analysis of embankment slope stability under the influence of water damage[14–19]. Practical achievements in the study of water hazards on embankment slopes mainly centered on the analysis of engineering cases and field experiments and proposed various risk assessment methods and early warning methods for water hazards[20–23]. However, at present, there is relatively little research on the mechanisms of embankment slope disaster induced by extreme rainfall in loess areas in theoretical terms.

Research on the prevention and treatment technologies for water hazards of embankment slopes has seen the evolution of slope reinforcement techniques from rigid support structures[24–26] such as soil nails, retaining walls or flexible supports like anchored piles and cable-frame systems[27–29]. However, for embankment slope disasters in railway engineering, traditional support structures commonly face issues such as long construction periods,

[1]Railway Engineering Research Institute, China Academy of Railway Sciences Corporation Limited, Beijing 100081, China. [2]National Key Laboratory of High-Speed Railway Track System, China Academy of Railway Sciences Corporation Limited, Beijing 100081, China. ✉email: 765197423@qq.com

high safety risks, and substantial project costs during emergency rescue and disaster relief efforts. Therefore, there is an urgent need to develop new technologies applicable to embankment slope disaster rescue.

This article took the embankment slope collapse disaster induced by extreme rainfall in Zhengzhou City, Henan Province, in July 2021 as the research object. Field disaster investigation, in-situ geotechnical tests, numerical simulation analysis, field monitoring tests, on-site pull-out tests, and surface wave detection tests were used to analyze the disaster mechanism and prevention technology of embankment slip-collapse in extreme rainfall conditions. The collapse mode of loess embankment slope was proposed, and the disaster mechanism of embankment slope collapse was studied. A new technology of steel grouting pipe suitable for the prevention and control of embankment slope collapse disasters in Zhengzhou loess area was developed. The effectiveness had been verified through surface wave detection, field monitoring tests, and numerical simulation, providing reference for reinforcement and treatment projects of railway embankment slopes in loess areas.

Characteristics of deterioration of loess strength in Zhengzhou in contact with water

The deterioration characteristics of loess strength in contact with water is the basis of the study of the mechanism of railway embankment slip-collapse disasters. Firstly, the test area was selected and the in-situ pressuremeter test was conducted to study the deterioration characteristics of shear modulus of loess in contact with water, and to propose a quantitative relationship between the shear modulus and moisture content. Secondly, the laboratory quick direct shear test was used to study the deterioration characteristics of cohesion and internal friction angle of Zhengzhou loess after water exposure.

Selection of the tested area

The loess in Zhengzhou city is mainly distributed in its western areas of Xingyang and Gongyi counties. In July 2021, the extreme rainfall severely affected the stability of the loess embankment slopes in Xingyang and Gongyi. Therefore, embankment in Xingyang and Gongyi where the railway passing through was selected as the tested area to study the characteristics of strength degradation of loess in contact with water. According to geological drilling surveys from multiple locations in the tested area, no groundwater has been exposed within a depth range of 40 m below the ground surface. The considerable depth of the phreatic zone in our study area eliminates hydrostatic pressure effects on slope mechanics.

Physical properties of the loess in Zhengzhou

Given that the total length of the railway in the tested area is 42 km, to study the physical properties of the loess, it is necessary to find out whether there are differences in the physical properties of loess along the railway. Therefore, multiple soil sampling points were selected in the tested area in Xingyang and Gongyi. Soil sampling points were determined along the railway at the interval of 2 km. Dry drilling was used to bore into the embankment slopes along the railway, and undisturbed samples were obtained using thin-walled soil samplers. A total of 90 samples were collected in Xingyang and 108 samples were collected in Gongyi to determine the physical properties of the loess, as shown in Table 1.

Statistical value Parameter		Sample size	Average value	Maximum values	Minimum value	Standard deviation	Variation coefficient	Correction factor	Standard deviation	Location
Moisture content ω	%	108	23.27	31.40	16.80	3.73	0.160	1.067	24.82	Xingyang
Relative density *ds*	–	108	2.71	2.72	2.70	0.01	0.004	0.999	2.70	
Natural density ρ	g/cm^3	108	1.97	2.07	1.86	0.06	0.031	0.987	1.93	
Dry density ρ_d	g/cm^3	108	1.60	1.69	1.44	0.07	0.046	0.981	1.56	
Void ratio *e*	–	108	0.69	0.891	0.597	0.085	0.121	1.050	0.744	
Saturation *Sr*	%	108	88.94	100.00	65.00	9.08	0.102	1.042	92.72	
Liquid limit ω_L	%	108	28.00	33.60	25.00	2.96	0.106	1.044	29.13	
Plastic limit ω_p	%	108	18.65	21.80	16.70	1.55	0.083	1.035	19.30	
Plasticity index I_p	–	108	9.35	13.00	7.80	1.57	0.170	0.929	8.60	
Liquidity index I_L	–	102	0.55	0.96	0.13	0.24	0.431	1.185	0.65	
Moisture content ω	%	90	24.35	32.40	21.50	3.152	0.129	1.060	25.81	Gongyi
Relative density *ds*	–	90	2.70	2.72	2.70	0.008	0.003	0.999	2.70	
Natural density ρ	g/cm^3	90	1.99	2.02	1.92	0.026	0.013	0.994	1.95	
Dry density ρ_d	g/cm^3	90	1.60	1.64	1.47	0.051	0.032	0.985	1.56	
Void ratio *e*	–	90	0.69	0.85	0.64	0.060	0.085	1.039	0.74	
Saturation *Sr*	%	90	92.20	100.00	87.00	4.632	0.050	1.023	94.33	
Liquid limit ω_L	%	90	28.02	33.80	25.30	2.530	0.091	1.042	28.89	
Plastic limit ω_p	%	90	18.89	21.30	17.30	1.267	0.067	1.031	19.47	
Plasticity index I_p	–	90	9.13	12.50	7.80	1.338	0.151	0.930	8.22	
Liquidity index I_L	–	90	0.62	0.98	0.30	0.190	0.309	1.142	0.70	

Table 1. Physical properties of loess in Xingyang and Gongyi area.

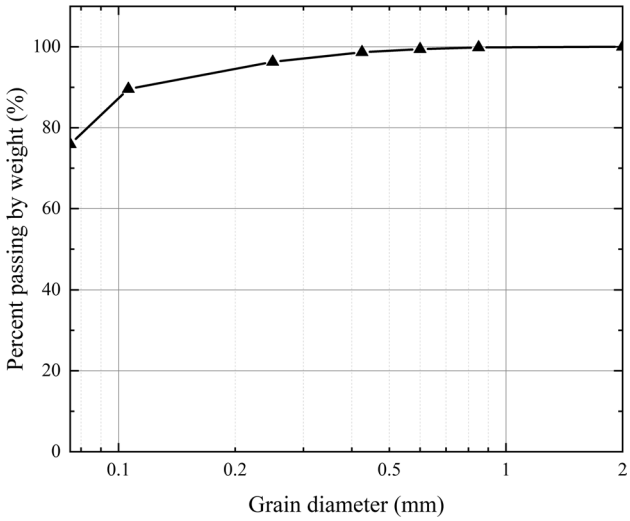

Fig. 1. Zhengzhou loess particle size distribution curve.

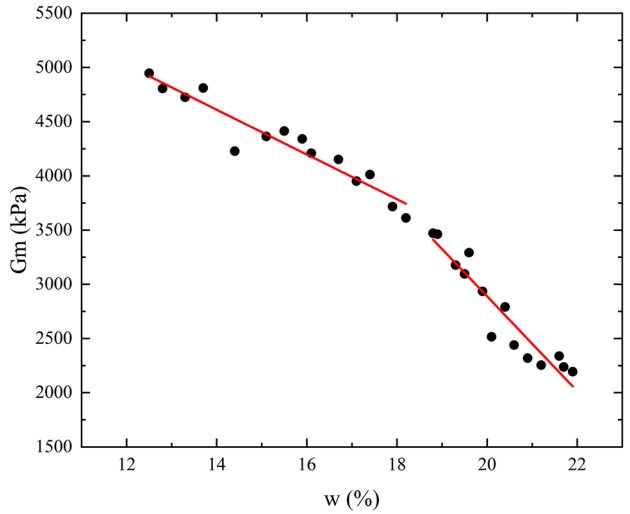

Fig. 2. Test area loess G_m-ω relationship distribution diagram.

The results indicated that there is no significant difference between the physical properties of loess in Xingyang and Gongyi. Except that the moisture content of the loess in Xingyang was higher than that in Gongyi, the dry density, porosity, and liquid-plastic limit of the loess were extremely close. Therefore, in the subsequent experimental research, the loess in Xingyang and Gongyi was no longer distinguished, and would be collectively referred to as the loess in Zhengzhou.

To scientifically classify soil and evaluate its physical properties, sieve analysis of the loess was carried out, and its particle size distribution (PSD) curve was depicted in Fig. 1, indicating that 100% of particles have passed through the 2 mm sieve, and 75.9% of particles have passed through the 0.075 mm sieve. According to the Unified Soil Classification System (USCS), the loess soil is silty clay since its plasticity index (PI) is between 7 and 17, and based on the plasticity chart from USCS, the loess soil plots near or slightly above the 'A-line', indicating it is silty clay.

Deterioration characteristics of the shear modulus of loess

After the extreme rainfall in July 2021, a pressuremeter test was conducted on the loess embankment slope in the experimental area. The natural moisture content of the soil was simultaneously measured to study the degradation characteristics of the shear modulus of loess with varying moisture content.

A total of 28 groups of pressuremeter tests were conducted at depths of 9–12 m below the ground surface. The relationship between shear modulus G_m and loess moisture content ω was shown in Fig. 2. It could be observed that as the moisture content increased gradually from 12.5%, the shear modulus indicated a decreasing trend. When the moisture content was below 18.5%, the rate of decrease was slow. However, when the moisture content

exceeded 18.5%, the rate of decrease in shear modulus accelerated. Therefore, a segmented linear regression method was employed to fit the relationship between shear modulus and loess moisture content, and the results were presented in Eqs. (1) and (2).

$$G_m = -206.3\omega + 7498.6\,(12.5 \le \omega(\%) < 18.5) \tag{1}$$

$$G_m = -437.0\omega + 11628.6\,(18.5 \le \omega(\%) < 21.9) \tag{2}$$

The segmented linear regression method yielded good fitting results. When $12.5\% \le \omega < 18.5\%$, the correlation coefficient R^2 was 0.91, and the rate of shear modulus decrease was: for every 1% increase in moisture content, the shear modulus decreased by 206.3 kPa. When $18.5\% \le \omega < 21.9\%$, the correlation coefficient R^2 was 0.89, and the rate of shear modulus decrease was: for every 1% increase in moisture content, the shear modulus decreased by 437.0 kPa.

The pressuremeter test was a horizontal load test, and the lateral expansion of flexible membrane compressed soil deformation, so the value of the shear modulus reflected the soil's resistance to lateral deformation. When the moisture content was lower than the plastic limit of 18.5%, the loess was in a semi-solid state and the soil was relatively hard. At this time, an increase in moisture content kept the soil in a semi-solid state, resulting in a slow rate of decrease in the shear modulus. When the moisture content exceeded 18.5%, the loess was in a plastic state and the soil hardness decreased. At this time, an increase in moisture content put the soil in a plastic state, leading to a significantly increased rate of decrease in the shear modulus.

Deterioration characteristics of the cohesion and the internal friction angle of loess

An indoor direct shear test on the loess in Zhengzhou was conducted. Rapid direct shear tests were performed to determine the strength parameters of silty clay under extreme moisture conditions, simulating undrained failure triggered by intense rainfall. Specimens were subjected to confining stresses of 100, 200, 300, and 400 kPa. The peak shear strength values, plotted against confining pressure, were analyzed via linear regression to derive cohesion (intercept) and internal friction angle (slope). Fifteen groups of loess samples with similar sampling depths, bulk densities, plastic limits, and liquid limits were selected for indoor humidification. Loess samples with target moisture contents of 12%, 16%, 20%, 24%, and 28% were prepared. The parameters of the tested soil samples were shown in Table 2.

The test results of cohesion and internal friction angle of loess samples at various moisture states were shown in Figs. 3 and 4. Deterioration characteristics of the cohesion and the internal friction angle of loess could be concluded as follows.

1) Both the cohesion and the internal friction angle of the loess in Zhengzhou decreased as the moisture content increased. As the moisture content increased from 11.2 to 28.0%, the cohesion of the loess decreased from 24.6 to 8.3 kPa, resulting in a decrease of 16.3 kPa and a loss of 66.26%. Meanwhile, the internal friction angle decreased from 21.8° to 19.8°, leading to a decrease of 2° and a loss of 9.17%.

2) When the moisture content approached the plastic limit, the cohesion of the loess in Zhengzhou experienced a sharp decline with the increase of moisture content. The trend of cohesion variation with moisture content was shown in Table 3. As the moisture content increased from 15.8 to 20.1%, the cohesion dropped sharply from 20.4 to 12.5 kPa, resulting in a decrease of 7.9 kPa. The proportion of cohesion loss at this stage accounted for 48.5% of the total loss, and the average rate of cohesion decrease was the highest, which was 1.84 kPa/%. The maximum rate of cohesion loss in this stage was due to the moisture content increasing from below the plastic limit to above the plastic limit. As shown in Table 2, the plastic limit range of loess samples ranged from 18.1 to 19.2%. As the moisture content increased from 15.8 to 20.1%, the thickness of the water film

Number	Moisture content (%)	Sampling depth (m)	Dry density ρ_d (g/cm^3)	Plastic limit (%)	Liquid limit (%)
S-12-1	11.2	6.1	1.61	18.8	27.9
S-12-2	11.6	6.3	1.61	18.4	28.1
S-12-3	11.9	6.7	1.61	18.9	28.4
S-16-1	15.4	6.3	1.60	18.1	27.9
S-16-2	15.8	6.4	1.61	18.6	28.4
S-16-3	15.9	6.9	1.60	18.8	28.2
S-20-1	19.7	7.4	1.60	19.0	28.4
S-20-2	19.8	6.5	1.60	18.4	27.9
S-20-3	20.1	6.7	1.60	19.0	28.0
S-24-1	24.2	6.9	1.60	19.0	28.3
S-24-2	24.6	7.3	1.60	18.6	27.9
S-24-3	25.1	7.1	1.60	19.1	28.4
S-28-1	27.6	7.4	1.62	19.0	28.0
S-28-2	27.7	6.9	1.62	19.2	28.3
S-28-3	28.0	7.1	1.62	19.0	28.3

Table 2. Tested loess parameters.

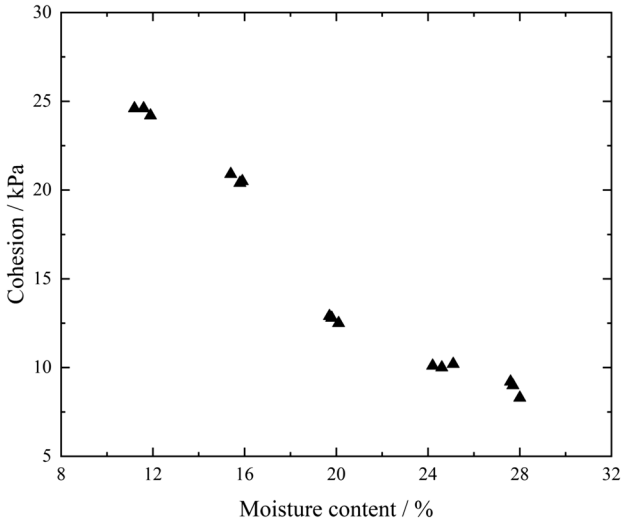

Fig. 3. Tested loess cohesion—moisture content diagram.

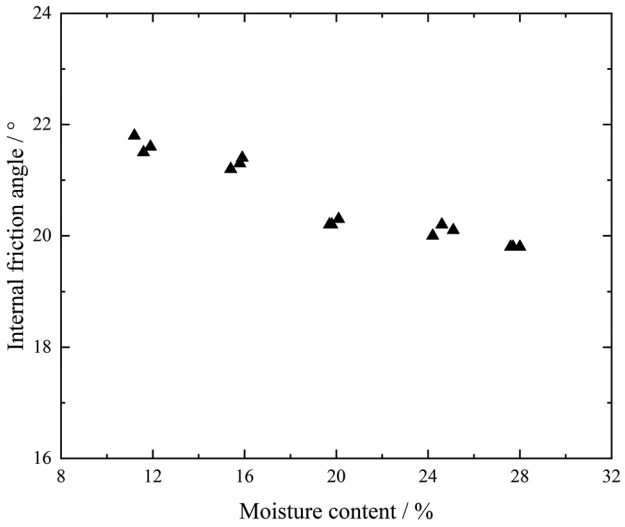

Fig.4. Tested loess internal friction angle—moisture content diagram.

Change in moisture content (%)	Change in cohesion (kPa)	Average rate of decrease in cohesion (kPa/%)
Increase from 11.2 to 15.8	Decrease from 24.6 to 20.4	0.91
Increase from 15.8 to 20.1	Decrease from 20.4 to 12.5	1.84
Increase from 20.1 to 24.2	Decrease from 12.5 to 10.1	0.59
Increase from 24.2 to 28.0	Decrease from 10.1 to 8.3	0.47

Table 3. Change trend of tested loess cohesion with moisture content in test area.

between loess particles increased significantly, and the bonding strength between particles decreased, resulting in a sharp decline in the cohesion of loess.

3) When the moisture content approached the plastic limit, the internal friction angle of the loess in Zhengzhou decreased abruptly with the increase of moisture content. The trend of internal friction angle variation with moisture content was shown in Table 4. As the moisture content increased from 15.8 to 20.1%, the internal friction angle decreased sharply from 21.3° to 20.3°, resulting in a decrease of 1°. The proportion of internal friction angle loss at this stage accounted for 50% of the total loss.

Change in moisture content (%)	Change in angle of internal friction (°)	Average rate of decrease in angle of internal friction (°/%)
Increase from 11.2 to 15.8	Decrease from 21.8 to 21.3	0.11
Increase from 15.8 to 20.1	Decrease from 21.3 to 20.3	0.23
Increase from 20.1 to 24.2	Decrease from 20.3 to 20.0	0.07
Increase from 24.2 to 28.0	Decrease from 20.0 to 19.8	0.05

Table 4. Change trend of tested loess internal friction angle with moisture content in test area.

Fig. 5. Embankment slope slip-collapse.

Mechanism of embankment slip-collapse

Embankment slip-collapse disasters seriously affect the safe operation of railways. Therefore, it is imperative to conduct in-depth research on their damage patterns and triggering mechanisms, which is significant to the efficient implementation of flood prevention work. In this section, the damage pattern of embankment slip-collapse was proposed, and its characteristic was analyzed based on field investigations. Subsequently, a numerical simulation method was used to study the disaster-causing mechanisms of embankment slip-collapse.

Failure mode of embankment slip-collapse

Embankment slip-collapse is a type of water-related hazard on the slope of an embankment. In this failure mode, water sources include surface runoff and atmospheric precipitation. Water seepages along the slope and acts on the shallow soil of the embankment slope, leading to the softening of the slope and eventual slip-collapse.

Characteristics of the failure

In the event of extreme rainfall, the drainage capacity of the embankment's top surface is insufficient, water flows continuously from the embankment's top surface to the lower part of the slope. Simultaneously, atmospheric rainfall directly affects the slope surface of the embankment. Without effective waterproofing measures on the slope surface of the embankment, precipitation easily seepages along the slope, softening the shallow soil under the slope surface. The softened soil experiences an increase in moisture content and a decrease in strength, resulting in the following characteristics of slope failure:

1. When the duration of rainfall infiltration on the slope is short, the shallow layer of soil on the slope surface softens. Soil with higher moisture content is in a liquid state, leading to the formation of slope mud flow under the erosion of surface runoff.
2. As the duration of rainfall infiltration on the slope increases, deeper layers of soil on the slope softens. Some of the weaker soils are stripped off the slope by scouring water, forming small-scale gullies on the slope surface.
3. With further increase in the duration of rainfall infiltration on the slope, deeper layers of soil on the slope become saturated. The entire surface layer of the slope exhibits a flowing state, resulting in slope slip-collapse. The thickness of the slope slip-collapse generally does not exceed 3 m.

A typical case analysis

The mud flow and the small-scale gully on the slope surface are still in the primary stage of water hazard development and do not affect the morphology of the embankment surface. Therefore, this section only focused on the analysis of a typical case of slope slip-collapse.

An embankment experienced slope slip-collapse, as shown in Fig. 5. Field investigations revealed that the shallow layer of soil on the slope surface softened due to water seepage and flowed downstream along the slope

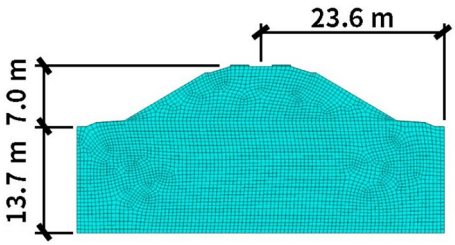

Fig. 6. Numerical calculation model.

Saturation	Density/kg·m^{-3}	Deformation modulus/MPa	Porosity	Saturated infiltration coefficient/cm·s^{-1}	Cohesive force /kPa	Internal friction angle/°	Poisson's ratio
0.54	1840	26.22	0.41	4.5×10^{-4}	22.6	21.4	0.30
0.65	1888	21.00	0.41	4.5×10^{-4}	20.0	21.1	0.32
0.77	1935	15.00	0.41	4.5×10^{-4}	13.0	20.4	0.34
0.88	1982	9.00	0.41	4.5×10^{-4}	12.0	20.2	0.38
1.00	2030	4.65	0.41	4.5×10^{-4}	10.2	20.0	0.40

Table 5. Soil parameter of embankment slope.

	Low-intensity seepage	Medium-intensity seepage	High-intensity seepage
Rainfall values (mm/d)	5	37	400
Seepage intensity (m/s)	5.78×10^{-8}	4.28×10^{-7}	4.63×10^{-6}

Table 6. Infiltration intensity value.

surface, leading to slope slip-collapse. The range of the slip-collapse extended from the toe of the embankment slope to the toe of the railway ballast. The shoulder protection net lost its foundation support, and eventually collapsed, causing severe damage to the vegetation on the slope.

Mechanism of embankment slip-collapse

Numerical simulation was conducted using an actual work site on the loess embankment slope along the railway experiencing water hazard as an example. Parameters such as the dimensions of the slope, the mechanical properties of the soil, and the boundary conditions were set appropriately to ensure that the slope's destruction process corresponds to the actual engineering conditions on site. Boundary conditions for water seepage were applied on the right side of the slope surface to simulate the deformation process of the slope under different infiltration intensities.

Numerical modeling

Based on the field investigation data, a numerical calculation model was established of the actual engineering case described in Section "A typical case analysis" (Fig. 6).

Calculation parameters and boundary conditions

The calculation parameters were determined by physical and mechanical tests such as the pressuremeter test mentioned in Section "Characteristics of deterioration of loess strength in Zhengzhou in contact with water", and the value of poisson's ratio is determined by previous study in the same tested area [30] The values of the soil parameters for the embankment slope were shown in Table 5.

As for the boundary conditions of numerical calculation model, firstly, horizontal and vertical displacement constraints are applied at the model base. Secondly, horizontal displacement constraints are applied to both sides of the foundation layer. Thirly, pore water pressure at the model boundaries is set to 0. Fourthly, the initial pore pressure throughout the model is set to 0. Finally, a seepage boundary was set on the right side of the embankment slope, and different values of seepage intensity were used for calculation to simulate the failure modes of the slope under different seepage conditions. The seepage intensity was determined with reference to the level of rainfall intensity. According to the Meteorological Law of the People's Republic of China, rainfall events can be divided into six levels based on daily rainfall: light rainfall (less than 10 mm/d), moderate rainfall (10.0–24.9 mm/d), heavy rainfall (25.0–49.9 mm/d), storm rainfall (50.0–99.9 mm/d), torrential rainfall (100.0–250.0 mm/d) and severe storm rainfall (more than 250.0 mm/d). Three calculation models of different seepage conditions were set: low-intensity seepage, medium-intensity seepage, and high-intensity seepage (Table 6). The low-intensity seepage was determined by the average intensity of light rain, while the medium-intensity seepage

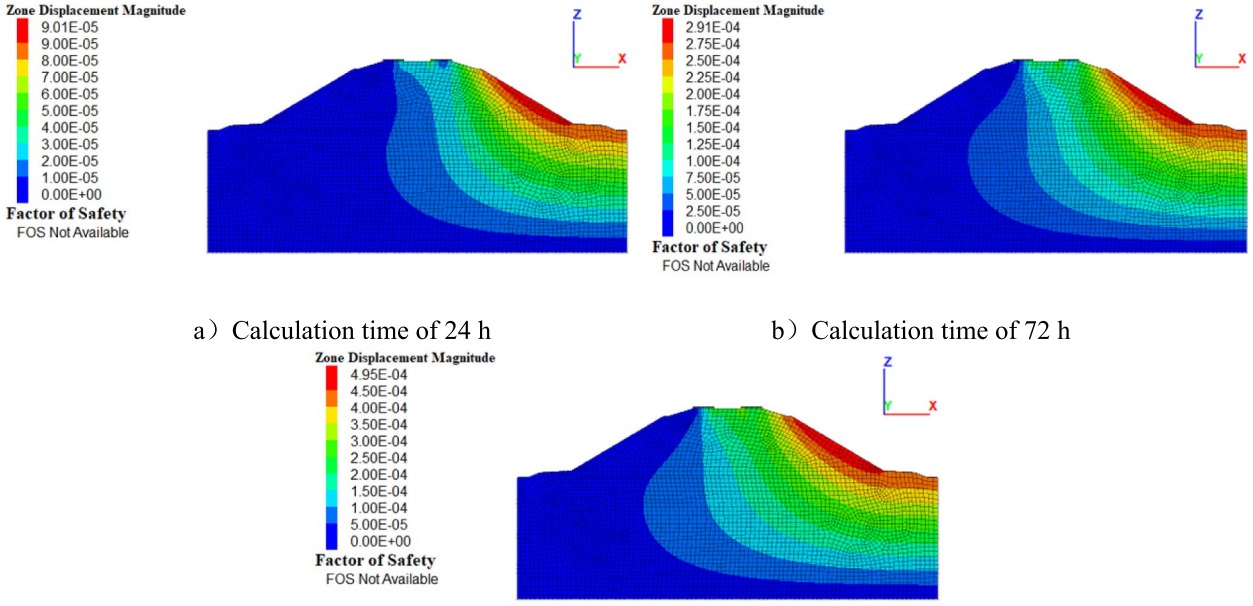

a）Calculation time of 24 h

b）Calculation time of 72 h

c）Calculation time of 120 h

Fig. 7. Magnitude displacement nephogram under low-intensity seepage condition.

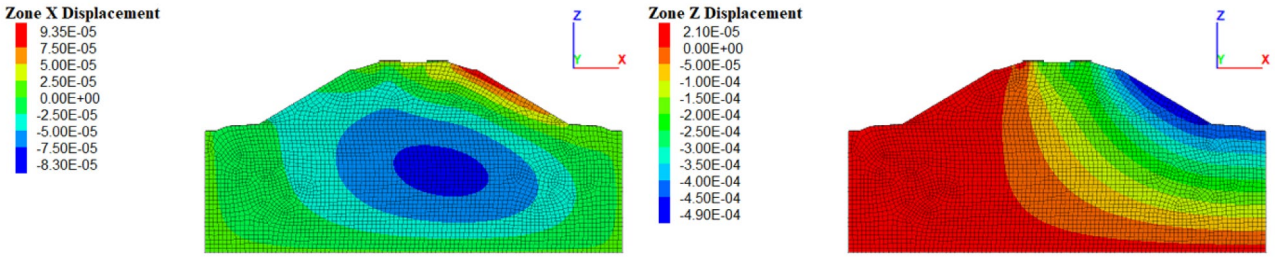

a）Horizontal displacement

b）Vertical displacement

Fig. 8. Displacement nephogram under low-intensity seepage condition.

was based on the average intensity of heavy rain, and the high-intensity seepage relied on the extreme rainfall intensity in Zhengzhou in July 2021.

Calculation results

(1) Low-intensity seepage condition

Figure 7 showed the magnitude displacement nephogram under low-intensity seepage condition. It could be seen from the figure that the distribution pattern of the magnitude displacement was basically consistent at different calculation times. The magnitude displacement of the right embankment slope affected by rainfall infiltration was larger. As time progressed, the magnitude displacement continued to increase, but the overall displacement value was relatively small. At the calculation time of 120 h, the maximum total displacement was only 0.049 cm.

The horizontal and vertical displacements at the calculation time of 120 h were extracted, as shown in Fig. 8. At the calculation time of 120 h, the entire right slope surface was the region of maximum horizontal and vertical displacements. The maximum values of horizontal and vertical displacements were 0.009 cm and -0.049 cm (negative values indicate settlement), indicating that the vertical displacement had a greater impact on the total displacement of the embankment.

As could be seen in Fig. 9, the maximum shear strain appeared on the right embankment slope under the influence of rainfall seepage. As time went on, the continuous effect of seepage caused the maximum shear strain to continuously develop downward along the slope. Under the low-intensity seepage condition, the maximum

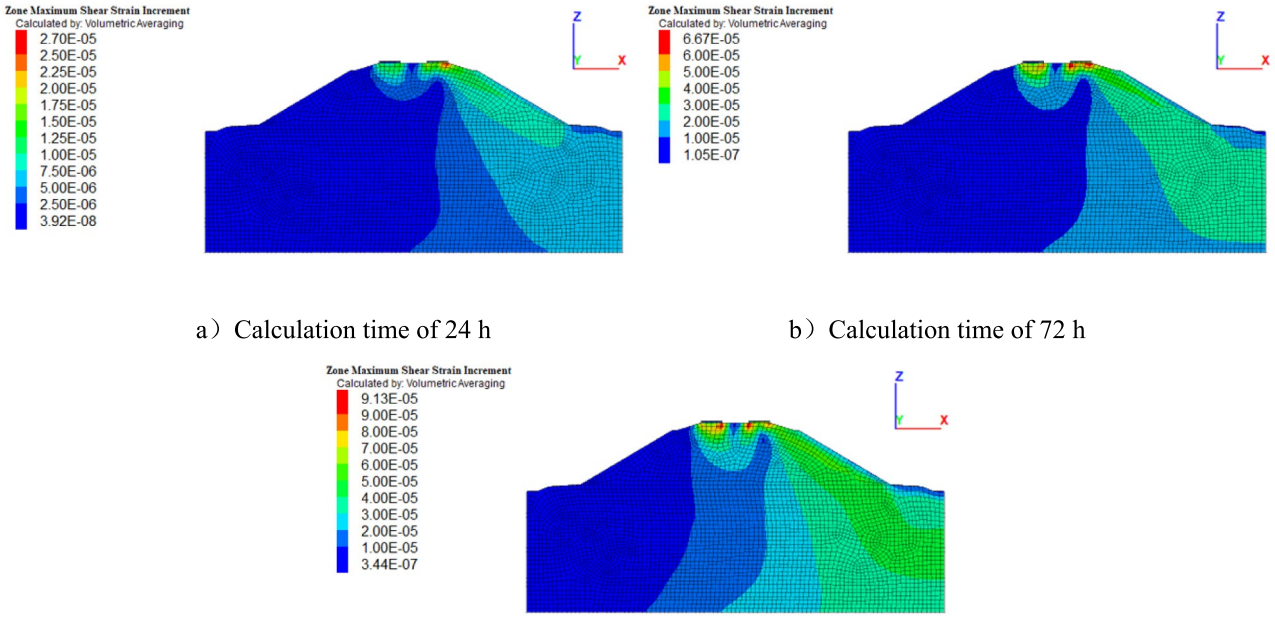

a）Calculation time of 24 h

b）Calculation time of 72 h

c）Calculation time of 120 h

Fig. 9. Maximum shear strain nephogram under low-intensity seepage condition.

value of shear strain on the slope was relatively small, and no slope slip-collapse was formed on the embankment slope.

(2) Medium-intensity seepage condition

As shown in Fig. 10, at the calculation time of 24 h, the maximum magnitude displacement appeared near the foot of the embankment on the right slope. With the continuous effect of seepage, the maximum value region expanded towards the upper part of the slope progressively. At the calculation time of 120 h, the maximum value region basically spanned through the entire right slope. The maximum magnitude displacement increased from 0.10 to 0.43 cm. The area primarily affected by rainfall seepage was the surface layer of the slope, and the total displacement continuously increased with the duration of seepage.

The horizontal and vertical displacement at the calculation time of 120 h were shown in Fig. 11. At this moment, the region of maximum vertical displacement covered the entire right slope surface, while the region of maximum horizontal displacement included the right slope surface and the top area of the embankment. Under the medium-intensity seepage condition, the area affected on vertical displacement by seepage was essentially consistent with that under low-intensity infiltration condition. However, the area affected on horizontal displacement by seepage expanded further to the top area of the embankment. The maximum values of horizontal and vertical displacements were 0.154 cm and − 0.397 cm (negative values indicate settlement). Compared with low-intensity seepage condition, both horizontal and vertical displacements increased significantly. Vertical displacement still had a greater impact on the magnitude displacement of the embankment.

Figure 12 illustrated the maximum shear strain nephogram under medium-intensity seepage condition. Under the effect of rainfall infiltration, maximum shear strain appeared at the toe of the right slope of the embankment at the calculation time of 24 h. Subsequently, as seepage continued, the area of maximum shear strain continuously expanded to the upper part of the slope. Under the medium-intensity seepage condition, the maximum values of both magnitude displacement and shear strain increased compared to the low-intensity seepage condition, but the values remained relatively small.

(3) High-intensity seepage condition

As shown in Fig. 13, due to the large amount of seepage, a significant region of extreme values of magnitude displacement quickly appeared on the right side of the embankment. At the calculation time of 24 h, the soil thickness of the extreme value region was approximately 0.5 m, with the maximum displacement reaching 2.71 cm. As time progressed, under the continuous action of seepage, the affected range of the extreme value region deepened continuously, and the maximum value of magnitude displacement kept increasing. At the calculation time of 120 h, the thickness of the extreme value region increased to 2.5 m approximately, and the maximum displacement increased to 12.30 cm. Compared to the medium-intensity seepage condition, the area affected by rainfall deepened further and the magnitude displacement continuously increased with the duration of seepage.

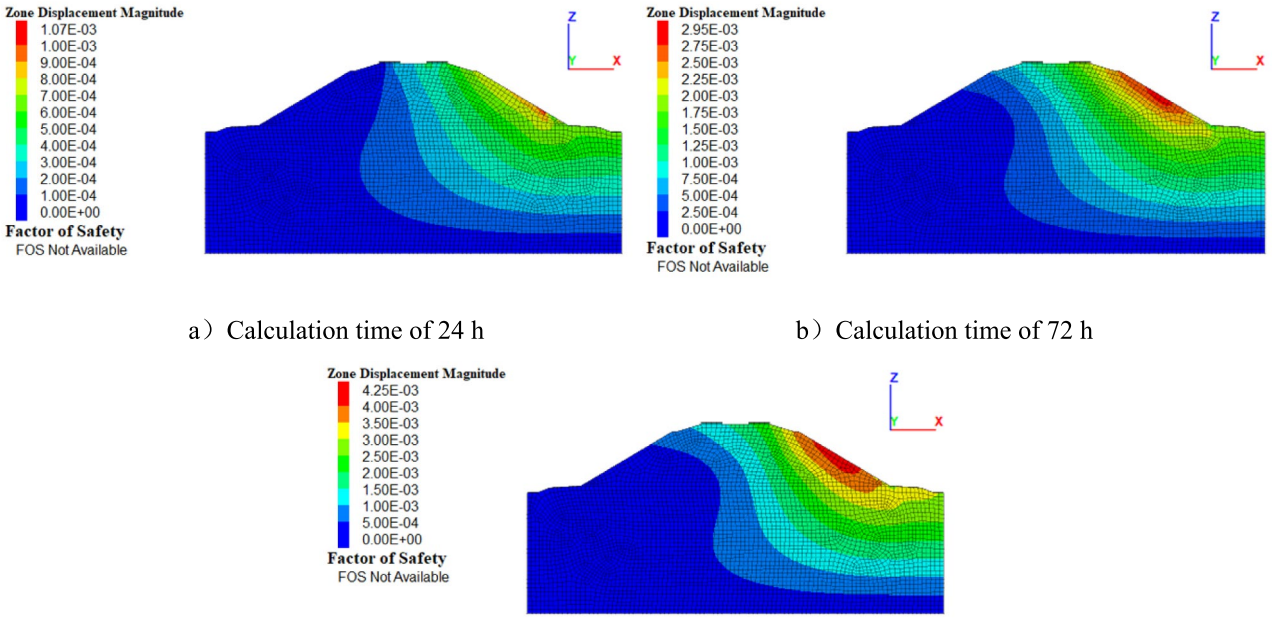

a）Calculation time of 24 h

b）Calculation time of 72 h

c）Calculation time of 120 h

Fig. 10. Magnitude displacement nephogram under medium-intensity seepage condition.

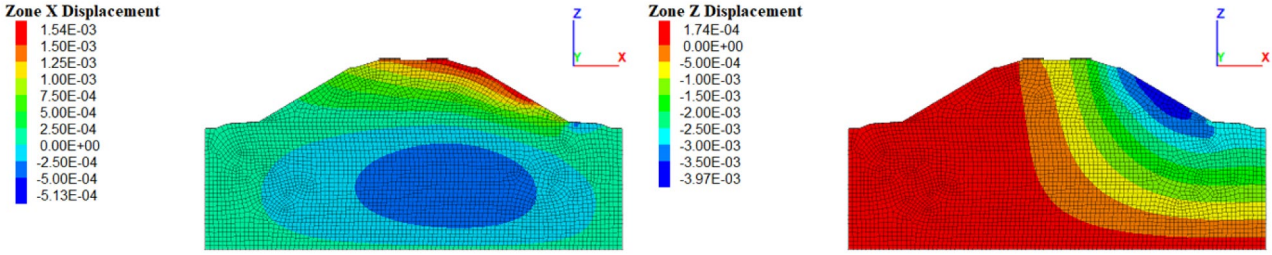

a）Horizontal displacement

b）Vertical displacement

Fig. 11. Displacement nephogram under medium-intensity seepage condition.

From Fig. 14, it could be observed that at the calculation time of 120 h, the influence of seepage on the horizontal and vertical displacements of the embankment was primarily on the right slope. The maximum values of horizontal and vertical displacement were 11.50 cm and − 8.25 cm, respectively (negative values indicate settlement). Compared to the previous two conditions, both horizontal and vertical displacement significantly increased. Besides, vertical displacement still had a greater impact on the magnitude displacement of the embankment.

Figure 15 displayed that under the influence of seepage, a region of maximum shear strain value quickly developed in the shallow layer of the right slope of the embankment. Under the high-intensity seepage condition, both the magnitude displacement and the maximum shear strain increased significantly, leading to the slip-collapse on the embankment slope.

(4) Analysis of stability coefficient

Strength reduction analysis was conducted on the soil of the embankment slope under low, medium, and high-intensity seepage conditions. As shown in Fig. 16, the stability coefficients of the embankment slope under low, medium, and high-intensity seepage conditions were 2.46, 1.82, 0.98 respectively. The stability coefficients that are larger than 1 indicate that the loess embankment slope has no potential for instability under low and medium-intensity seepage conditions, while the stability coefficient that is less than 1 demonstrates that the loess embankment slope is in instability state under the high-intensity seepage condition.

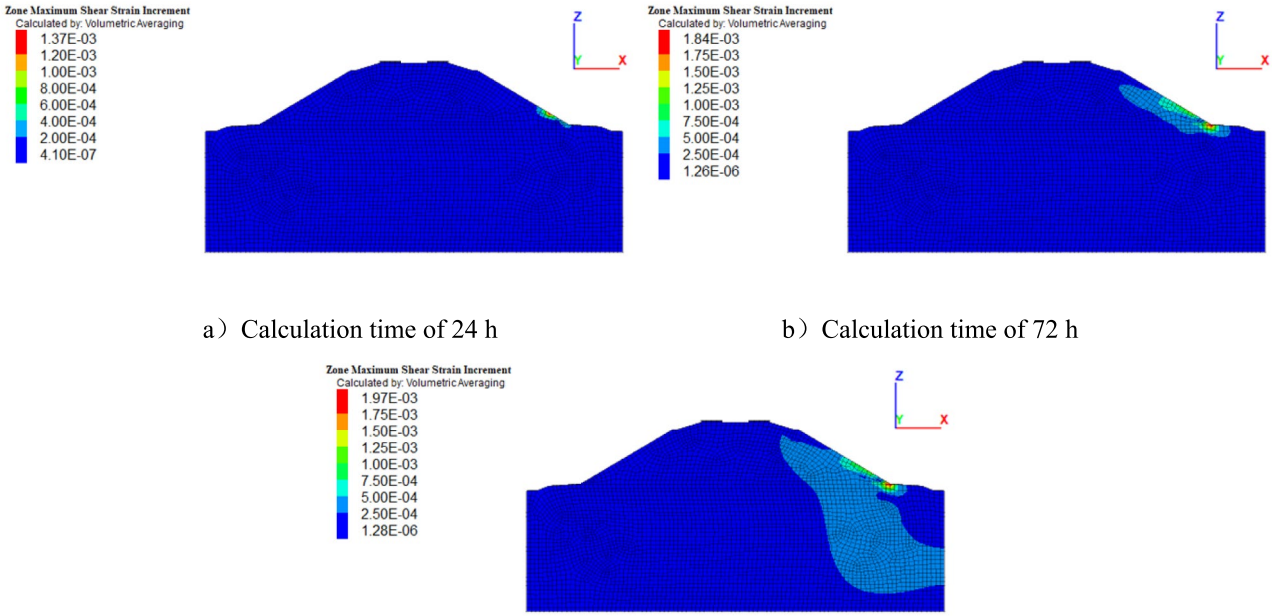

a）Calculation time of 24 h

b）Calculation time of 72 h

c）Calculation time of 120 h

Fig. 12. Maximum shear strain nephogram under medium-intensity seepage condition.

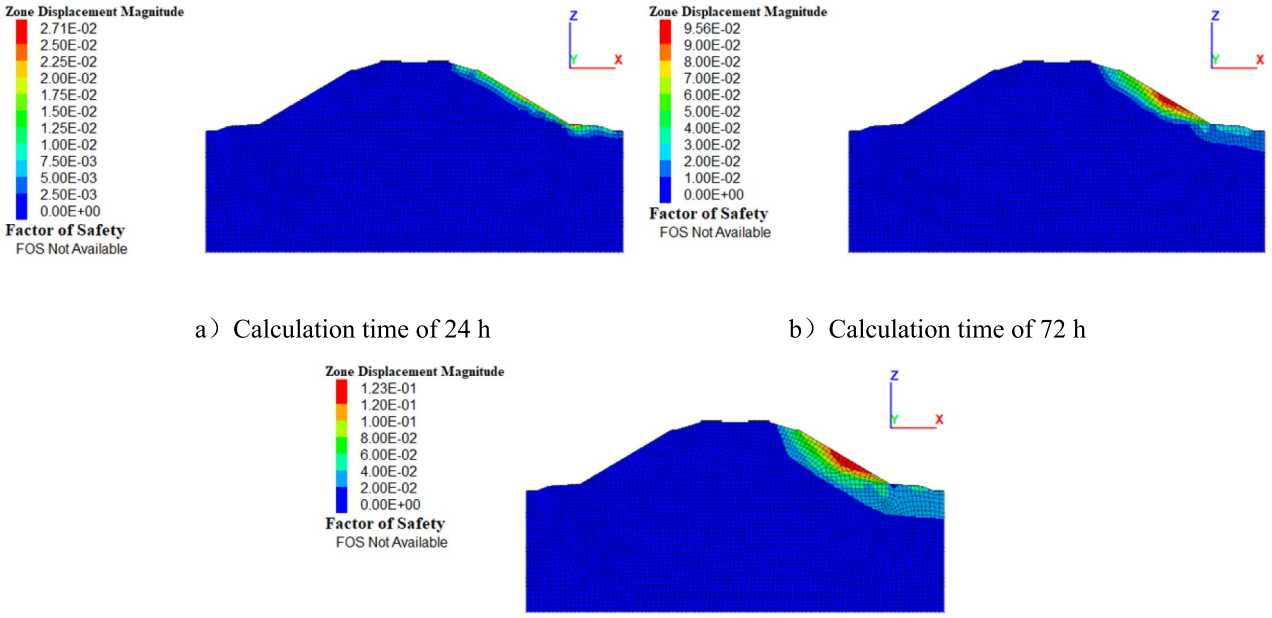

a）Calculation time of 24 h

b）Calculation time of 72 h

c）Calculation time of 120 h

Fig. 13. Magnitude displacement nephogram under high-intensity seepage condition.

(5) Analysis of seepage range

To analyze the seepage range of the embankment slope under different seepage conditions, saturation nephogram at the calculation time of 120 h for each condition were extracted (Fig. 17). It could be observed that at the calculation time of 120 h, the range of seepage mainly developed in the relatively shallow layer of the right slope under low-intensity seepage condition. The depth of soil saturation was approximately 0.6 m thick

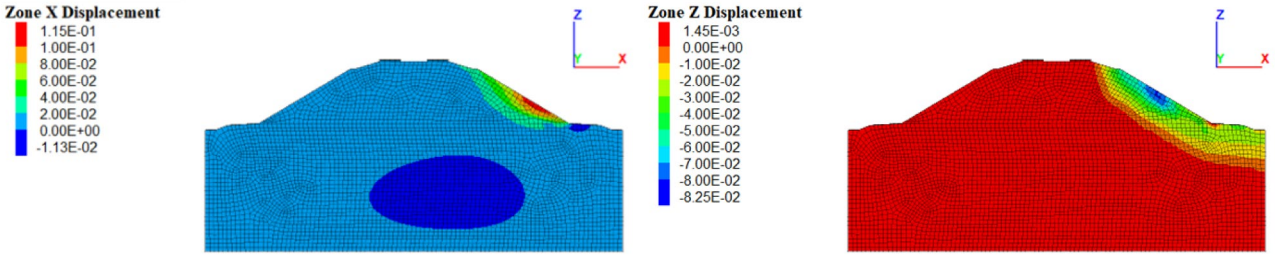

a）Horizontal displacement　　b）Vertical displacement

Fig. 14. Displacement nephogram under high-intensity seepage condition.

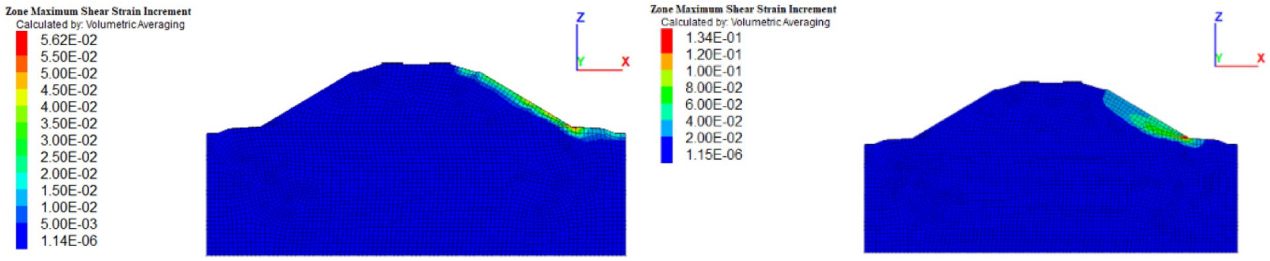

a）Calculation time of 24 h　　b）Calculation time of 72 h

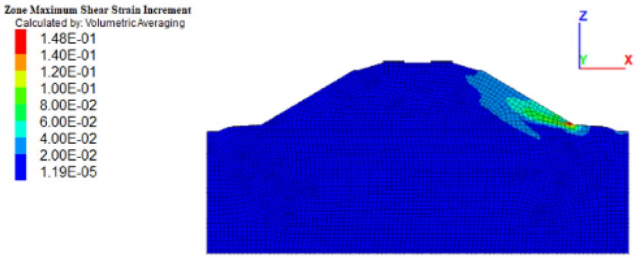

c）Calculation time of 120 h

Fig. 15. Maximum shear strain nephogram under high-intensity seepage condition.

below surface layer, with the corresponding soil saturation of 25.0–34.9%. As the seepage intensity increased, the depth of seepage also increased, with the depth of the soil infiltrated by rainwater rising continuously. Under medium-intensity seepage condition, the depth of the soil infiltrated by rainwater increased to 2.0 m, with the corresponding soil saturation increasing to 60.0–81.7%. Under the high-intensity seepage condition, the depth of the soil infiltrated by rainwater increased further to 3.0 m, with the corresponding soil saturation increasing to 90.0–100.0%. As the seepage intensity increased, the infiltrating water could not quickly flow along the slope surface, but could only seep deeper into the embankment slope, leading to a continuous increase in the depth of seepage and soil saturation.

The analysis was based on the results of the previous in-situ pressuremeter tests and numerical simulations. For loess with a relative density of 2.71 and a void ratio of 0.687, under low-intensity seepage condition, the soil saturation ranged from 25.0 to 34.9%, with corresponding soil moisture content ranging from 6.34 to 8.85%. At this point, the soil moisture content was relatively low, resulting in higher shear modulus, cohesion, and internal friction angle. Consequently, the total displacement of the slope was small, and there was no slip on the embankment slope. Under medium-intensity seepage condition, the soil saturation ranged from 60.0 to 81.7%, with corresponding soil moisture content ranging from 15.21 to 20.71%. In this condition, the shear modulus ranged from 4.36 to 2.58 MPa, the cohesion ranged from 20.9 to 12.5 kPa, and the internal friction angle ranged from 21.2° to 20.3°. Under high-intensity seepage condition, the soil saturation ranged from 90.0 to 100.0%, with corresponding soil moisture content ranging from 22.82 to 25.35%. The corresponding soil shear modulus,

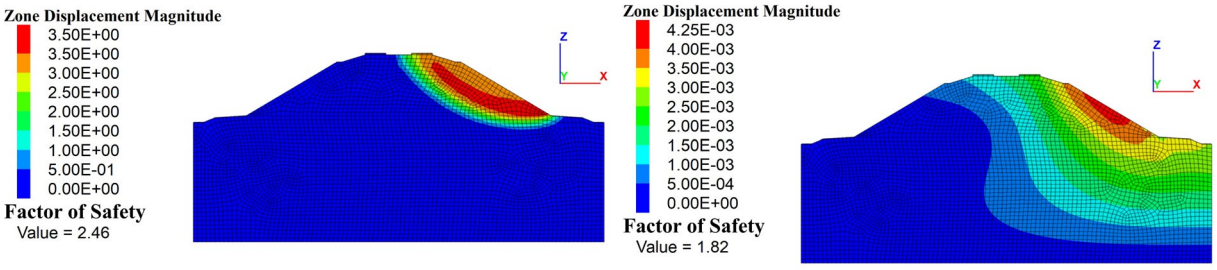

a）Calculation time of 24 h　　b）Calculation time of 72 h

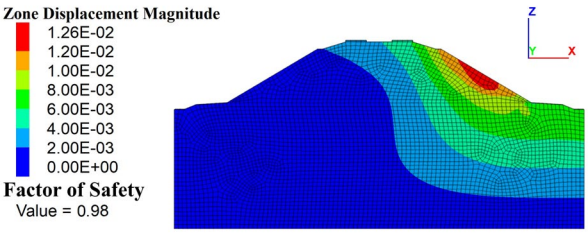

c）Calculation time of 120 h

Fig. 16. Maximum shear strain nephogram under high-intensity seepage condition.

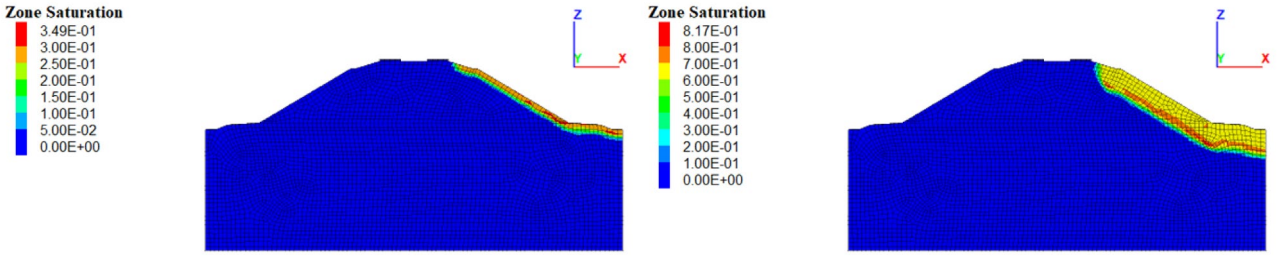

a）Low-intensity seepage condition　　b）Medium-intensity seepage condition

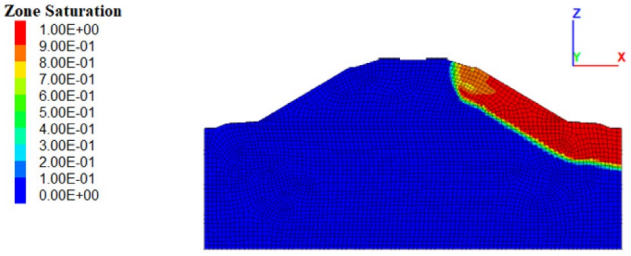

c）High-intensity seepage condition

Fig. 17. Saturation nephogram at the calculation time of 120 h.

cohesion and internal friction angle further reduced. Meanwhile, the soil shear strength reduced to less than the shear stress, and the embankment slope formed a slip-collapse.

Prevention technology of embankment slip-collapse

At present, the prevention technologies of embankment slopes primarily focus on drainage measures and slope protection measures. In the loess area of Zhengzhou, the shape and the ratio of some slopes do not meet the requirements of the current design specifications. As a result, serious slope slip-collapse disasters occur after

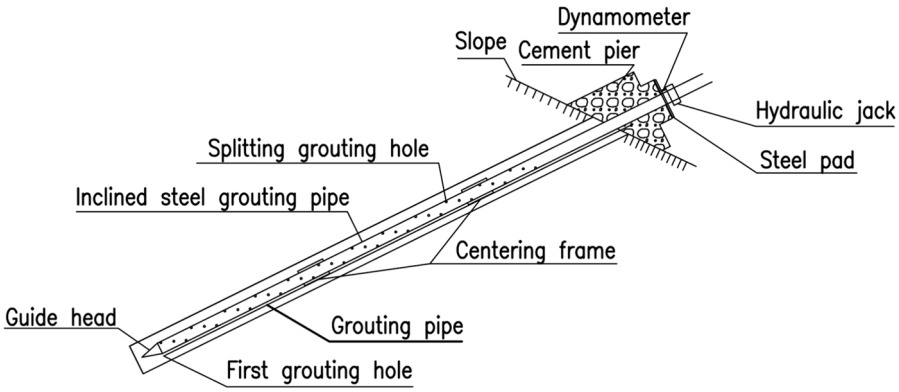

Fig. 18. Structure diagram of steel grouting pipe with multiple stage control grouting.

Fig. 19. In-situ testing equipment.

extreme rainfall, which can further induce overall slope instability. Therefore, in addition to drainage and slope protection measures, anchoring measures also need to be considered. However, loess is prone to collapse when it is encountered with the water, which can lead to insufficient anchoring force. Considering that anchor rods are difficult to meet the anchoring capacity requirements of anchoring projects, there is an urgent need to develop new prevention technology.

The new technology of steel grouting pipe with multiple stage control grouting

Steel grouting pipe with multiple stage control grouting is a new type of prevention technology that combines splitting grouting with anchoring engineering. The steel grouting pipe itself serves not only as a protective measure but also as a conduit for multiple stage control grouting. This technology utilizes splitting grouting to fill the cracks in the loess strata and compacting the surrounding soil mass around the drilling hole. The bonding strength of the grouting body and the loess strata increases, enhancing the anchoring force of the grouting steel grouting pipe in the loess strata. The structural diagram of this new technology is shown in Fig. 18.

Anchoring force test of steel grouting pipe on loess embankment slope

The anchoring capacity of steel grouting pipe with multiple stage control grouting in loess stratum is still uncertain. In order to investigate its anchoring force for reinforcing loess slopes, an on-site pull-out test was conducted on the loess embankment slope in the experimental area.

Test equipment

The pull-out test was conducted on a series of steel grouting pipes with a total anchorage length of 12 m. The steel pipe was a seamless steel pipe with dimensions of Φ60mm × 5mm. The equipment for the pull-out test included steel bearing plates, vibrating string dynamometers, and hydraulic jacks. The on-site test equipment is shown in Fig. 19.

Loading and unloading cycles	Load increment: percentage of ultimate tensile strength													
Cycle 1	10							30						10
Cycle 2	10	30						40					30	10
Cycle 3	10	30	40					50				40	30	10
Cycle 4	10	30	40	50				60			50	40	30	10
Cycle 5	10	30	40	50	60			70		60	50	40	30	10
Cycle 6	10	30	40	50	60	70		80	70	60	50	40	30	10
Cycle 7	10	30	40	50	60	70	80	90						
Observation time(min)	5	5	5	5	5	5	5	15	5	5	5	5	5	5

Table 7. Steel grouting pipe pull-out test loading and unloading grade table.

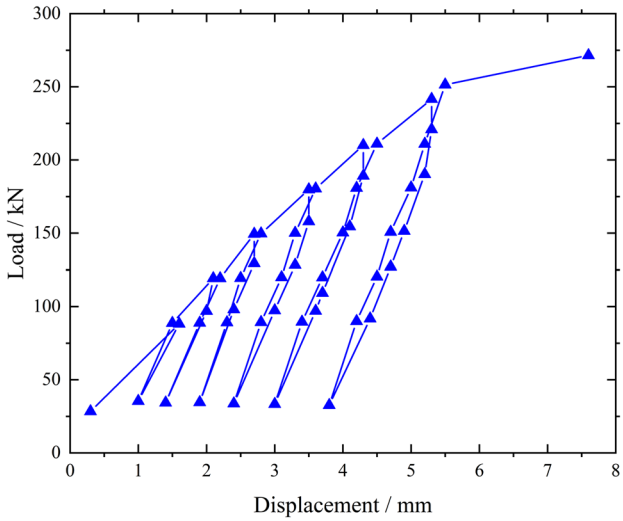

Fig. 20. Pull-out test curve of steel grouting pipe of group 1.

Test method

The test employed the cyclic loading and unloading method, using hydraulic jacks to apply and remove loads on the steel grouting pipe. The loading and unloading levels for the pull-out test were presented in Table 7.

Test result

Two parallel sets of tests were conducted to obtain the pull-out test curves, as shown in Figs. 20 and 21.

The results in Fig. 20 indicated that the displacement of the steel grouting pipe could still converge when the load was applied up to 251 kN. However, when the load increased to 271 kN, the displacement increment caused by the subsequent load level twice that caused by the previous load level, suggesting that the displacement was no longer convergent. Therefore, the anchoring force obtained from the first set of pull-out tests was 251 kN.

The results in Fig. 21 indicated that the displacement of the steel grouting pipe could still converge when the load was applied up to 251 kN. When the load increased to 268 kN, the displacement increment caused by the subsequent load level twice that caused by the previous load level, indicating that the displacement is no longer convergent. Therefore, the anchoring force obtained from the second set of pull-out tests was also 251 kN.

Effectiveness of steel grouting pipe on the reinforcement of loess embankment slopes

To explore the effectiveness of the new steel grouting pipe technology for preventing slip-collapse disasters on loess embankments, the surface wave test, field monitoring test, and the numerical simulation were conducted to evaluate the effectiveness of the grouting reinforcement.

Surface wave test

The Rayleigh surface wave imaging method is a shallow surface exploration technique, which is very suitable for evaluating the reinforcement effectiveness of surface slope diseases. By measuring the velocities of surface waves at different frequencies and analyzing the relationship between wave velocity and frequency, the properties of stratum at various depths could be deduced consequentially.

(1) In-situ test line layout

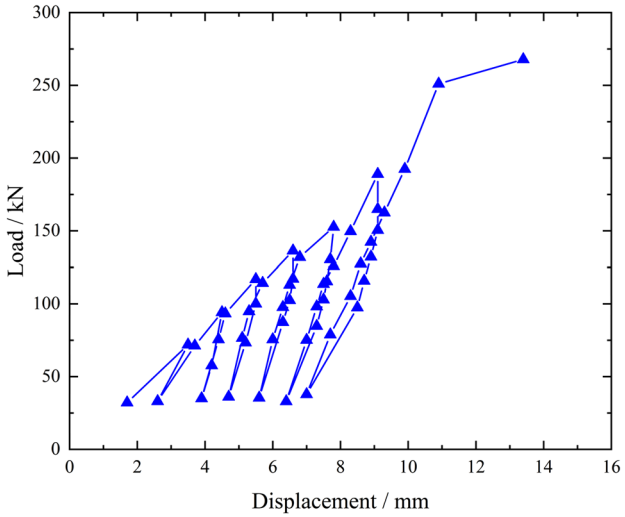

Fig. 21. Pull-out test curve of steel grouting pipe of group 2.

a）Before grouting b）2 months after grouting

Fig. 22. Diagram of in-situ test line layout.

The tests set up a pair of inspection profiles parallel to the direction of the railway line, with a length of 80 m. Detectors were placed at intervals of 2 m. The tests were conducted both before grouting and two months after grouting. The in-situ test line layout was shown in Fig. 22.

(2) Test result

As shown in Fig. 23, before grouting, there were areas of low wave velocity in the depth range of 0–9 m at 10–25 m along the profile direction, in the depth range of 0–3 m at 25–45 m along the profile direction, in the depth range of 0–10 m at 45–50 m along the profile direction, and in the depth range of 0–5 m at 50–70 m along the profile direction. The wave speed in these areas ranged from 135 to 246 m/s. It was speculated that these low wave velocity values were related to the low compactness of the loess in these areas.

There were areas of low wave velocity in the depth range of 7–9 m at 28–35 m along the profile direction, and in the depth range of 13–17 m at 52–53 m along the profile direction. The wave speed in these areas ranged from 186 to 263 m/s. It was speculated that the loess desiccation cracks were well-developed in these regions, with local voids present.

As shown in Fig. 24, two months after grouting, there was a zone of low wave velocity in the depth range of 0–1 m at 10–25 m along the profile direction. The wave velocity in this area ranged from 169 to 255 m/s, which represented an increase compared to that before grouting. Notably, the area of low-velocity zone at 10–25 m along the profile direction had decreased compared to that before grouting. Meanwhile, there was a significant increase in velocity in the depth range of 1–9 m, with a wave velocity ranging from 220 to 340 m/s. The wave velocity was about 100 m/s higher than that before grouting.

The area of low-velocity zone in the depth range of 0–3 m at 25–45 m along the profile direction had decreased significantly. The wave velocity within the region increased, with a velocity range of 237–417 m/s, representing an increase of 100 to 200 m/s compared to that before grouting.

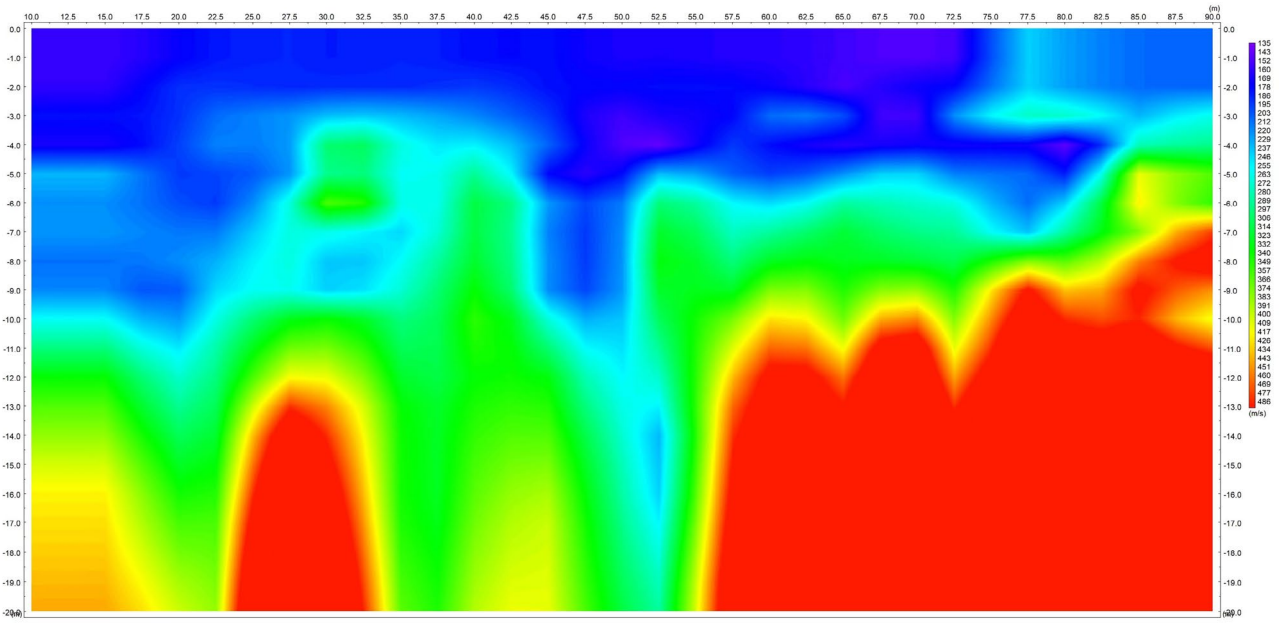

Fig. 23. Wave velocity interpretation results before grouting.

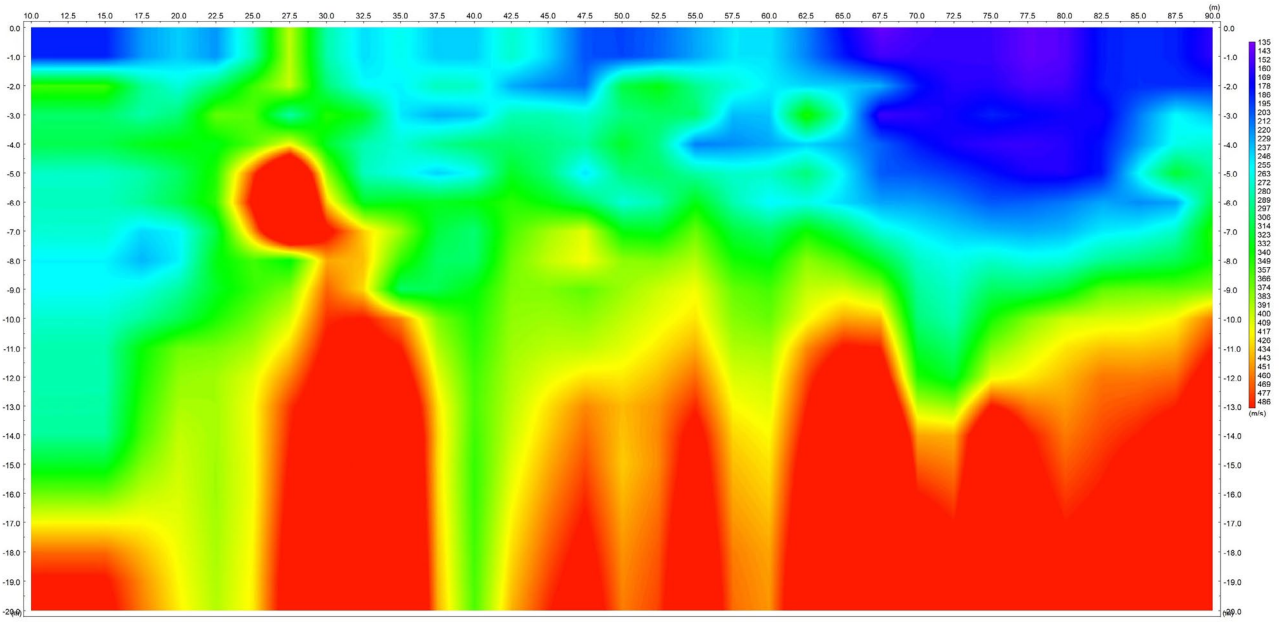

Fig. 24. Wave velocity interpretation results 2 months after grouting.

There was a low wave velocity area in the depth range of 0-w m at 45–50 m along the profile direction. The wave velocity in this area ranged from 178 to 263 m/s, increasing a lot compared with that before grouting. It was worth noting that the area of low-velocity zone at 45–50 m along the profile direction had decreased compared to that before grouting. Besides, there was a significant increase in velocity in the depth range of 2–10 m, with a wave velocity ranging from 289 to 417 m/s. The wave velocity was about 150 m/s higher than that before grouting.

The area of low-velocity zone in the depth range of 0–5 m at 50–65 m along the profile direction had decreased significantly. The wave velocity within the region increased, with a velocity range of 178–314 m/s, representing an increase of about 50 m/s compared to that before grouting.

Two months after grouting, there were areas of high wave velocity in the depth range of 7–9 m at 28–35 m along the profile direction, and the depth range of 13–17 m at 52–53 m along the profile direction. The wave

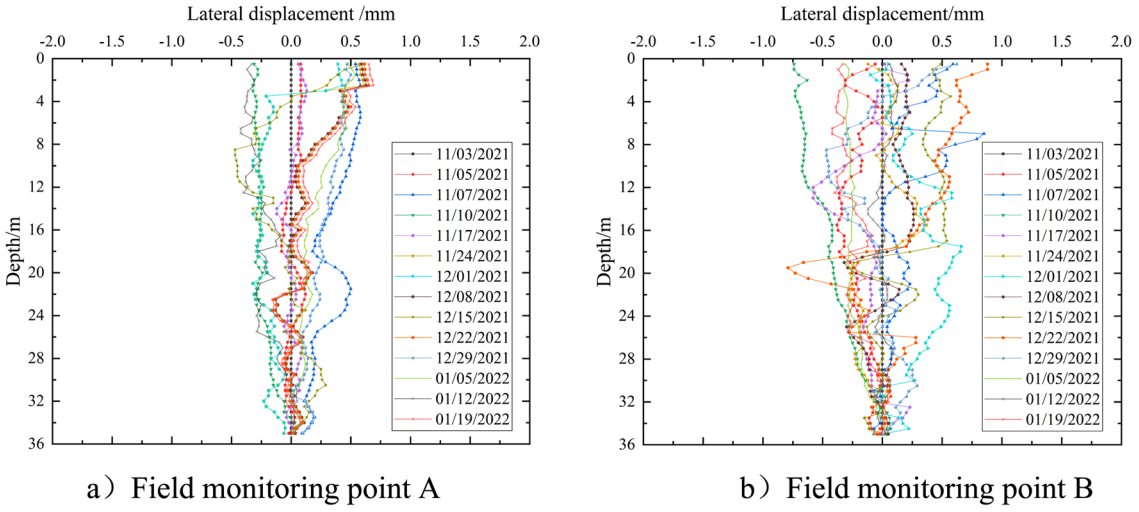

Fig. 25. Field monitoring results after reinforcement.

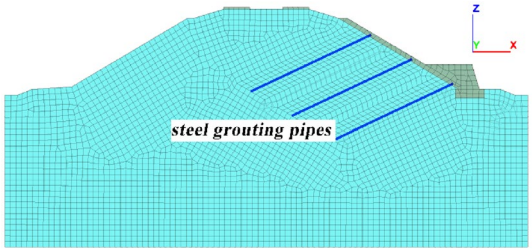

Fig. 26. Numerical calculation model after reinforcement.

velocity in these regions ranged from 426 to 486 m/s, representing an increase of over 200 m/s compared to before grouting. The results indicated that the cracks and the local voids had been improved after grouting.

Field monitoring test

To verify whether the stability of the embankment slope has been improved after reinforcement, field monitoring measures of displacement inclinometer were employed. As shown in Fig. 25, from November 2021 to January 2022, the overall lateral displacement of the embankment slope was minimal, with lateral displacements less than 1 mm. Therefore, it is concluded that the reinforced embankment slope is in a stable state after reinforcement.

Numerical simulation

To evaluate the effectiveness of the new technology of steel grouting pipe in slope reinforcement, numerical simulation was conducted on the embankment slope reinforced by steel grouting pipe. The deformation characteristics of the embankment slope under high-intensity seepage condition were analyzed.

(1) Numerical modeling

The numerical calculation model was established according to the engineering case described in Section "A typical case analysis". Three rows of steel grouting pipes were installed on the slope surface, and a C30 retaining wall was placed at the foot of the slope. The steel grouting pipes were connected by crown beams to form an integral structure. The numerical calculation model after reinforcement was shown in Fig. 26.

(2) Calculation parameters

According to the results of the field test, the soil within 1 m around the steel grouting pipes was affected by the splitting grouting. Based on the mechanical tests of loess after splitting grouting reinforcement, cohesion of the effected soil increased to 35 kPa, and internal friction angle of the effected soil increased to 23°. The physical and mechanical parameters of the soil that were not affected by grouting could be found in Table 5. The material parameters for the crown beam and the steel grouting pipes were shown in Table 8. In the numerical model, the soil was simulated by ideal elastoplastic materials, which conformed to the Mohr–Coulomb yield criterion. Additionally, the crown beams and the steel grouting pipes were simulated by elastic materials.

	Density/kg·m^{-3}	Elastic modulus/MPa	Poisson's ratio
Crown beam	2360	3.00e4	0.20
Steel grouting pipe	7850	2.06e5	0.20
Retaining wall	2360	3.00e4	0.20
Backfill	1800	15	0.30

Table 8. Crown beams and steel grouting pipe parameters.

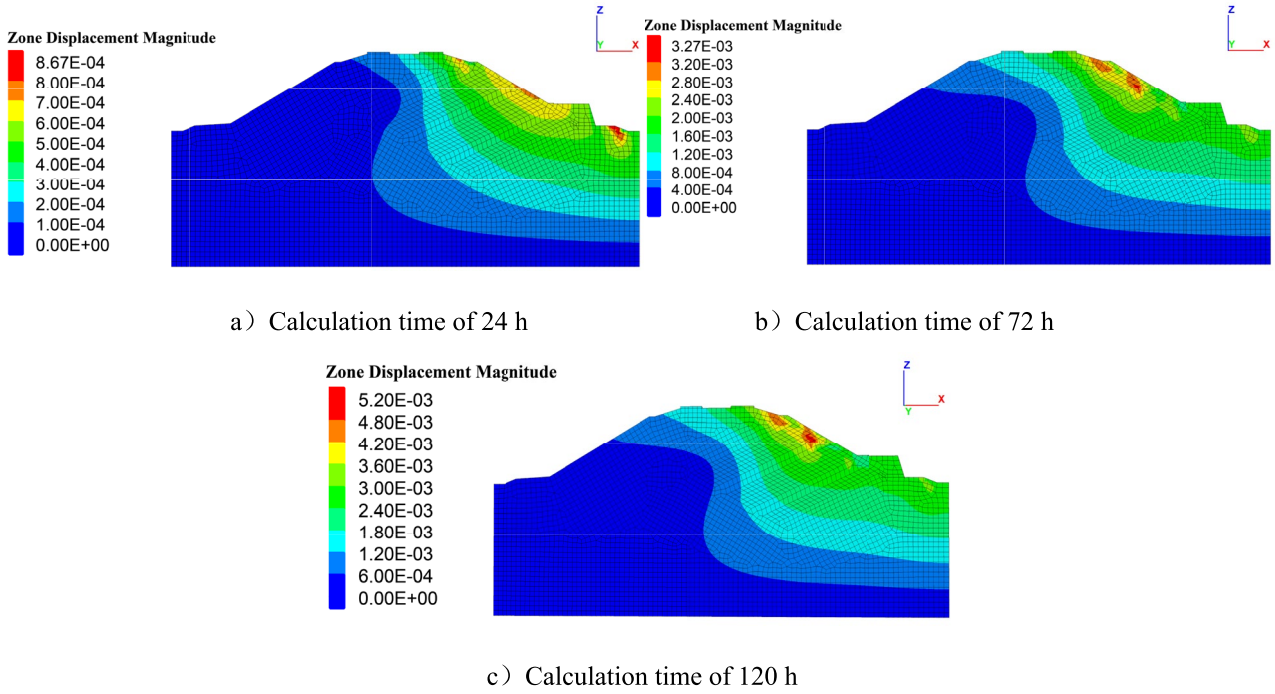

Fig. 27. Magnitude displacement nephogram under high intensity seepage condition after reinforcement.

(3) Calculation results

(1) Analysis of displacements

As shown in Fig. 27, after splitting grouting, the grouted cement spread to a radius of 1 m around the pipes. The solidification of the grouted cement reduced the permeability of the soil. Together with the restraining effect of the steel grouting pipes as well as the retaining wall, displacement of the embankment slope reduced significantly. At the calculation times of 24 h, 72 h, and 120 h, the maximum magnitude displacement of the embankment were 0.87 mm, 3.27 mm, and 5.20 mm, respectively. At the calculation time of 120 h, compared to the scenario without reinforcement measures, the maximum magnitude displacement had decreased by 11.78 cm, representing a reduction of 95.77%.

Figure 28 showed the horizontal and vertical displacements at the calculation time of 120 h. The influence of seepage on the horizontal and vertical displacements of the embankment mainly focused on the right side of the slope where rainfall seepage happened. The maximum values of horizontal and vertical displacements were 3.63 mm and − 4.46 mm, respectively (a negative value indicates settlement). Compared to the condition without reinforcement measures, both horizontal and vertical displacements had significantly decreased, demonstrating a noticeable improvement in reinforcement effectiveness.

(2) Analysis of maximum shear strain

As shown in Fig. 29, an area of maximum shear strain quickly formed in the shallow part of the right-side slope of the embankment under the influence of seepage. After that, as the seepage continued, the area of maximum shear strain expanded constantly. The area with the largest values of shear strain primarily concentrated in the region where the steel grouting pipes connected with the crown beam. Meanwhile, due to the effect of the retaining wall at the foot of the slope, the shear strain did not develop continuously to the foot of the slope, preventing the formation of a slope surface collapse.

(3) Analysis of stability coefficient

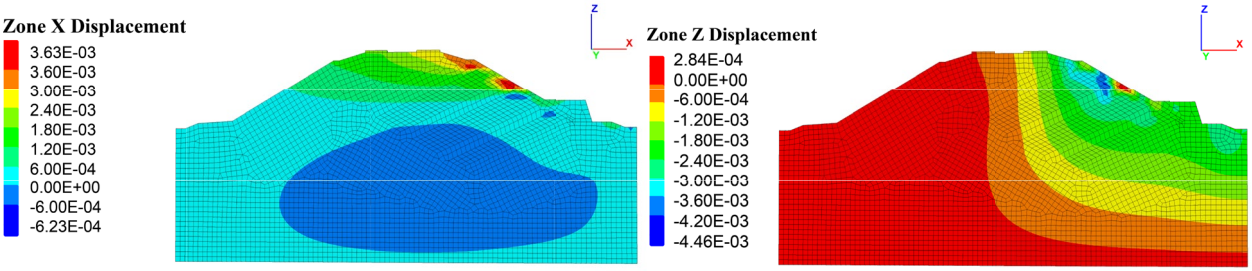

a）Horizontal displacement　　b）Vertical displacement

Fig. 28. Displacement nephogram under high intensity seepage condition after reinforcement.

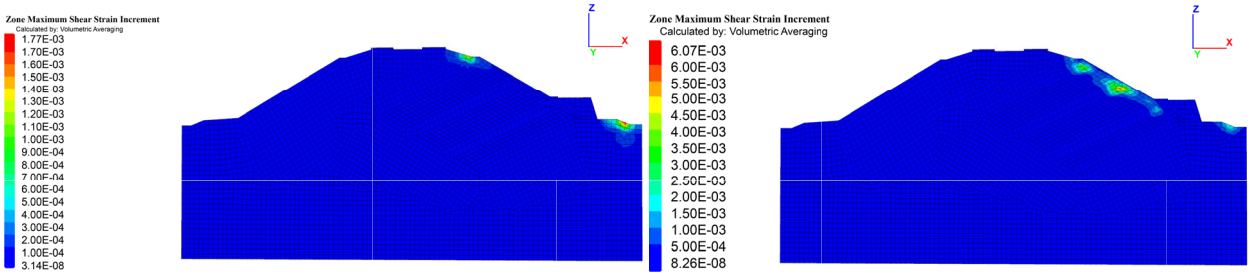

a）Calculation time of 24 h　　b）Calculation time of 72 h

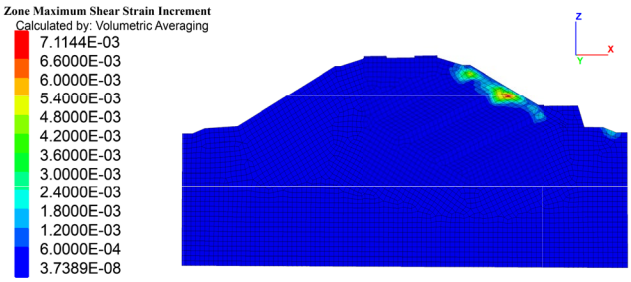

c）Calculation time of 120 h

Fig. 29. Maximum shear strain nephogram under high intensity seepage condition after reinforcement.

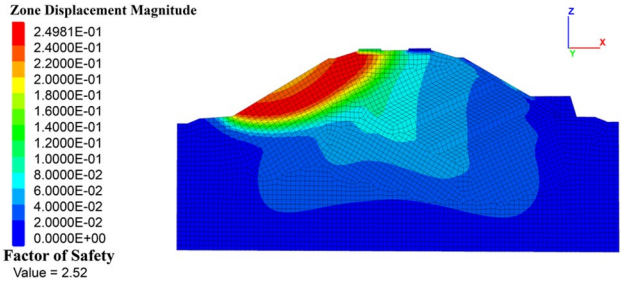

Fig. 30. Magnitude displacement nephogram of embankment instability after reinforcement.

Strength reduction analysis was conducted on the soil of the embankment slope under this condition and the displacement distribution was examined during the instability of the slope, as shown in Fig. 30. The stability coefficient of the embankment slope was 2.52, indicating that the combination of steel grouting pipes and retaining wall enhanced the stability of the slope. At the same time, the slope failure occurred on the left side of

the slope rather than the right side. Thus, the failure at this time was not caused by seepage, demonstrating that the reinforcement measures had a significant effect on strengthening the slope.

Discussion

Reinforcement principle

Based on extensive analysis of loess embankment slope failure mechanisms, this study proposes a comprehensive reinforcement principle integrating "Slope Drainage—Material Enhancement—Force Equilibrium Adjustment". The tripartite instability mechanism reveals that embankment slope failures primarily stem from three interrelated factors, which are hydro-mechanical erosion, progressive deterioration of loess mechanical properties, and critical exceedance of sliding forces.

Conventional reinforcement methods exhibit functional limitations by addressing singular aspects of this complex interaction. Surface drainage systems primarily mitigate superficial water infiltration but lack capacity for soil parameter modification. Permeation grouting techniques improve soil strength through particle cementation yet demonstrate negligible hydrological regulation effects. Structural countermeasures like anti-slide piles provide localized force redistribution without addressing moisture-sensitive property degradation. These compartmentalized approaches fail to resolve the coupled hydro-mechanical failure mechanisms inherent in loess embankments.

The proposed steel grouting pipe system achieves integrated functionality through three synergistic mechanisms. High-pressure grout injection induces controlled fracturing within the loess, generating interconnected cementitious networks that simultaneously divert subsurface water flow while creating impermeable barriers against capillary migration. Concurrent particle cementation and matrix densification processes enhance key geotechnical parameters. The embedded structural components provide distributed anchorage forces through soil-pipe interaction mechanisms, delivering both passive restraint against translational movement and moment resistance capacity for embankment stability.

Comparison of existing study results with this study results

This investigation establishes a hydro-mechanical failure mechanism for loess embankments, centering on drainage inadequacy during extreme precipitation events that triggers coupled seepage-softening synergism, accompanied by tri-phase evolutionary modeling. The proposed framework is systematically compared with contemporary research.

From the aspect of scientific merit, the tri-phase progressive failure model of 'shallow softening → scouring and stripping → overall flow' is proposed, which is consistent with the hydraulic erosion-shear compound failure theory of loess slope proposed by Zhou et al.[31]. Additionally, the thickness of 3 m is observed in this study when the embankment slope undergoes slip-collapse, which approximately conforms to the findings of Li. et al. [32], stating that the railway embankment was damaged to a depth of 3.1 m under the action of seepage-creep coupling.

In terms of theoretical innovation, the embankment slip-collapse mechanism proposed in this study innovatively integrates the synergistic mechanism of surface runoff scouring and internal seepage softening, breaking through the limitation of separating the two in traditional analysis [33–35].

As for implementation potential, the proposed 'shallow softening → scouring and stripping → overall flow' morphological evolution sequence provides a new dimension for quantitative evaluation of the degree of damage.

To summarize, the proposed mechanism of loess embankment slope collapse shows significant advantages in terms of scientific merit, theoretical innovation, and implementation potential.

Analysis of potential limitations of numerical model

The assumptions made in numerical model boundary conditions for simulating rainfall infiltration in embankment slopes indeed lead to discrepancies between simulated and realistic results. These discrepancies primarily are caused by simplified treatments of rainfall processes, soil–water coupling effects, as well as interaction between boundary conditions and material models.

In terms of the simplification of rainfall boundary conditions, real rainfall intensity varies in time and space, while simplified numerical simulation models assume constant values. This simplification can lead to overestimation or underestimation of infiltration in localized areas. Besides, simplified models neglect surface runoff, ignoring runoff's impact on slope stability.

As for the simplification of soil–water coupling effects, soil permeability coefficients change with moisture content in realistic conditions. However, simplified models assume constant permeability coefficients, potentially leading to imprecise estimates of infiltration rates.

Regarding the simplification of interaction between boundary conditions and material models, stress path changes induced by rainfall infiltration may trigger nonlinear soil behavior. However, simplified boundary conditions may prevent the model from accurately capturing these complex stress–strain relationships.

Analysis of influence of soil moisture content to embankment stability

According to the field test data and numerical simulation results, the influence of soil moisture content changes on the stability of embankment slope indicates significant nonlinear characteristics, and its core mechanism is reflected in the degradation law of shear strength parameters and the attenuation characteristics of shear modulus. The following quantitative analysis is conducted from the perspective of the change law of clay mineral microstructure and slope stability coefficient with the increase of moisture content.

From the perspective of the change law of clay mineral microstructure, when the moisture content approaches the plastic limit (18.1–19.2%), the thickness of the water film between soil particles changes suddenly from a monolayer (< 3Å) to a multilayer (> 10Å), which shows a similar result concluded by Pezowicz and Choma-

Moryl [36], claiming that for every 1% increase in moisture content between clay mineral layers, the specific surface area decreases by 12.7 m^2/g. Therefore, the change in the law of clay mineral microstructure plays a fundamental role in the degradation of soil properties, which counters for the decrease of embankment stability.

Comprehensive analysis of the deterioration law of soil shear strength parameters and shear modulus with increasing moisture content obtained from field tests and the slope stability change characteristics in numerical simulation results indicate that the slope stability can be divided into three intervals according to the moisture content. The first is the metastable zone, with a moisture content range of 15.21–20.71%, at which the shear modulus is 4.36–2.58 MPa. The cohesion is 20.9–12.5 kPa, and the internal friction angle is 21.2°–20.3°. The coefficient of embankment stability is 1.0–1.05. The second is the critical instability zone, with a moisture content range of 20.71–22.82%. The coefficient of embankment stability is around 1.0. The last is the instability zone, with a moisture content range of 22.82–25.35%. The coefficient of embankment stability is less than 1.0.

Advantages of splitting grouting technology utilizing steel grouting pipes

The fundamental mechanism underlying water-induced damage on loess embankment slopes stems from localized strength reduction in the loess material, where diminished shear strength fails to counteract applied shear stresses, ultimately leading to slope shear failure. To enhance loess strength parameters, various technical inventions are routinely implemented in engineering practice. Among these, splitting grouting technology has gained widespread adoption for rapid post-damage rehabilitation of railway embankments, owing to its minimal structural disturbance, operational convenience, and high mechanization potential, which has obvious advantages compared with filling grouting, permeation grouting, and compaction grouting.

Filling grouting primarily addresses subsurface voids including cavities. This technique involves injecting grout through fissure networks to occupy void spaces within the geotechnical matrix, thereby preventing water infiltration and enhancing overall impermeability through cavity filling.

Permeation grouting is typically applied to porous, fractured geological formations. The process relies on slurry migration through interconnected pore spaces, displacing pore water and air to form a cementitious matrix that reinforces the soil skeleton and improves geomechanical properties.

Compaction grouting widely applies in well-drained sandy soils. Utilizing high-viscosity grouts under controlled pressure, this method induces soil densification through radial displacement, promoting drainage consolidation and subsequent bearing capacity enhancement.

Splitting grouting demonstrates broad stratigraphic applicability. The technique involves high-pressure slurry injections that induce controlled shear failure. Initial grout penetration forms primary fracture channels, followed by secondary splitting grouting under sustained pressure, ultimately creating intricate root-like reinforcement networks that provide structural reinforcement through three-dimensional skeletal support systems.

Comparison of field monitoring or investigation results with numerical simulation results

Comparing the numerical simulation results with in-situ monitoring results, it turns out that they are in high consistency. The maximum magnitude displacement of the embankment after reinforcement is 0.87 mm under heavy rainfall conditions of 24 h, which is consistent with the actual field monitoring results, with lateral displacements less than 1 mm. This simulation result has accurately reflected the embankment slope deformations under the actual rainfall condition in rainy seasons of 2022–2024. Additionally, comparing the numerical simulation results with in-situ investigation results, it turns out that they are in high consistency. The thickness of the slope slip-collapse does not exceed 3 m before reinforcement under heavy rainfall conditions of 120 h, which is consistent with the actual field investigation results, with the thickness of the extreme value region of 2.5 m at the calculation time of 120 h. This simulation result has accurately reflected the embankment slope collapse zone thickness under the actual rainfall condition in rainy seasons of 2021. Therefore, it turns out that the numerical model is validated by proving that numerical model results are compatible with corresponding in-situ monitoring results and field investigation results.

Long-term sustainability

The implemented reinforcement scheme of steel grouting pipes achieved prompt stabilization of slope deformation, effectively supporting emergency rehabilitation of a 40 km section of the Railway and mitigation of over 150 embankment slope failures following the catastrophic July 2020 extreme rainfall event. The line was successfully reopened within 15 days, ensuring uninterrupted railway operations while yielding substantial socioeconomic benefits through minimized service disruption. Post-reinforcement monitoring through three consecutive rainy seasons (2022–2024) demonstrates sustained slope stability, with deformation rates maintained below 2 mm/year as per geodetic survey records.

Limitations of study

This paper proposes the mechanism of loess embankment slope collapse and develops a new splitting grouting technology, which provides a new theoretical framework for the prevention and control of disasters in loess areas. However, there are still the following deficiencies in the experimental design and analysis process.

The first limitation is lack of quantification of material interface effects. The influence of the microstructure of the interfacial transition zone (ITZ) between the steel grouting pipe and the loess has not been quantified. The mechanical characteristics of anchoring interface and load transfer mechanism are supposed to be investigated and analyzed in the future.

The second limitation is lack of investigation of dynamic response mechanism of steel grouting pipes. Although previous efforts by our research group have conducted thorough experimental research on the bearing capacity and effective anchorage length of steel grouting pipe on loess embankment slope[37], the on-site pull-out

test is a static load test and does not consider the impact of train dynamic load. The next step is to carry out high-frequency cyclic shear tests to establish a cumulative damage model.

Conclusions

The findings of this study on embankment slip-collapse in loess areas following extreme rainfall have significant implications for the broader field of geotechnical engineering, particularly in enhancing the stability of railway embankments. The research highlights the critical relationship between moisture content and the mechanical properties of the loess, demonstrating that moisture levels exceeding the plastic limit can lead to substantial degradation in shear strength. This insight is crucial for developing effective early warning systems and preventive measures against slope failures in similar geotechnical contexts. Additionally, the splitting grouting technology of steel grouting pipes proposed in this study can successfully and effectively reinforce loess embankment slope, providing a new structure for the reinforcement design of embankment slopes in loess areas. The results indicate:

(1) Laboratory investigations employing direct shear test revealed a sharp reduction in both cohesion and internal friction angle of loess as moisture content increased from 15.8 to 20.1%. Pressuremeter tests demonstrated a critical moisture content threshold of 18.5% where the rate of shear modulus degradation accelerated substantially. These findings indicate that surpassing the plastic limit initiates a critical phase where further moisture content enhancement triggers accelerated degradation of key mechanical parameters.
(2) Embankment slip-collapse, a geohazard characterized by shallow failures in slope surfaces, is primarily triggered by hydro-mechanical coupling under extreme rainfall. Inadequate surface drainage capacity and insufficient anti-seepage measures promote preferential infiltration along the slope, inducing softening of the subsurface soil.
(3) Numerical simulations reveal rainfall-induced seepage intensity is the dominant control of embankment stability. Comparative analysis demonstrates that slope deformation under high-intensity seepage of 24-h duration exceeds that observed under moderate-intensity conditions of 120-h duration.
(4) Three stages of slope stability division criteria are proposed, namely metastable zone, critical instability zone, and instability zone. The critical threshold of moisture content of 20.71% under these conditions provides a quantifiable benchmark for early warning systems targeting surface collapse prevention.
(5) An experimental investigation into the anchoring efficacy of steel grouting pipes in loess strata revealed significant performance enhancements. A 12-m-long pipe demonstrated an anchoring capacity of 251 kN. Surface wave velocity measurements, conducted two months post-grouting, indicated an increase exceeding 200 m/s compared to pre-grouting conditions, suggesting effective reinforcement of cracks and voids in the loess. Complementary field monitoring and numerical simulations corroborated the steel grouting pipe's ability to constrain displacement, mitigate maximum shear strain, and augment overall slope stability.

Data availability

The data that support the findings of this study are available on request to the corresponding author, [Wenjiao Zhou], upon reasonable request.

Received: 4 June 2024; Accepted: 29 May 2025
Published online: 01 July 2025

References

1. Ye, Z., Liu, X., Dong, Q., Wang, E. & Sun, H. Hydro-damage properties of red-bed mudstone failures induced by nonlinear seepage and diffusion effect. *Water* **14**(3), 351 (2022).
2. Wang, H. et al. Investigation of hydro-mechanical behaviour of excavation induced damage zone of callovo-oxfordian claystone: Numerical modeling and in-situ experiment. *Rock Mech. Rock Eng.* **55**(10), 6079–6102 (2022).
3. Zhou, C. et al. Coupled seepage and stress model and experiment verification for creep behavior of soft rock. *Int. J. Geomech.* **20**(9), 04020146 (2020).
4. Hong, B. et al. Using the meteorological early warning model to improve the prediction accuracy of water damage geological disasters around pipelines in mountainous areas. *Sci. Total Environ.* **889**, 164334 (2023).
5. Lu, T., Liu, S. D., Wang, B., Wu, R. X. & Hu, X. W. A review of geophysical exploration technology for mine water disaster in China: Applications and trends. *Mine Water Environ.* **36**, 331–340 (2017).
6. Xuanming, H., Yan, Z., Wensong, L. I. & Zenglin, T. I. A. N. Summary of water disaster characteristics and water prevention and control technology in open-pit coal mines in China. *Coal Geol. Explor.* **48**(4), 9 (2020).
7. Li, H. et al. A cascade disaster caused by geological and coupled hydro-mechanical factors—water inrush mechanism from karst collapse column under confining pressure. *Energies* **10**(12), 1938 (2017).
8. Zhang, Y. Preliminary analysis of geological disaster and water circulation system. In *E3S Web of Conferences* (Vol. 194, p. 04031). EDP Sciences (2020).
9. Binti Sa'adin, S. L., Kaewunruen, S. & Jaroszweski, D. Heavy rainfall and flood vulnerability of Singapore-Malaysia high speed rail system. *Austral. J. Civ. Eng.* **14**(2), 123–131 (2016).
10. Berg, H. P. Risks and consequences of weather hazards on railway infrastructure. *J. Pol. Saf. Reliabil. Assoc.* **8** (2017).
11. Liu, K., Wang, M., Cao, Y., Zhu, W. & Yang, G. Susceptibility of existing and planned Chinese railway system subjected to rainfall-induced multi-hazards. *Transp. Res. Part A Policy Pract.* **117**, 214–226 (2018).
12. Ridho, B. M. A. & Kaewunruen, S. Failure investigations into interspersed railway tracks exposed to flood and washaway conditions under moving train loads. *Eng. Fail. Anal.* **129**, 105726 (2021).
13. Raj, M. & Sengupta, A. Rain-triggered slope failure of the railway embankment at Malda, India. *Acta Geotech.* **9**, 789–798 (2014).
14. Bhadiyadra, K. & Ong, D. E. Mechanics of rainfall-induced landslides after a prolonged dry period based on laboratory tests and numerical models incorporating soil-water characteristic curves. *Geosciences* **14**(7), 174 (2024).
15. Hayano, K. Model tests and numerical analyses on the mechanism of flow-out of railway ballasts induced by flood inundation. *Jpn. Geotech. Soc. Spec. Publ.* **2**(46), 1636–1639 (2016).
16. Xu, S. & Zsáki, A. M. Maximum safe freight train speed on railway embankments under rapid drawdown conditions based on coupled stress-seepage slope stability analysis. *Transp. Geotech.* **27**, 100486 (2021).

17. Pan, Y., Wu, G., Zhao, Z. & He, L. Analysis of rock slope stability under rainfall conditions considering the water-induced weakening of rock. *Comput. Geotech.* **128**, 103806 (2020).
18. Hou, X., Vanapalli, S. K. & Li, T. Water infiltration characteristics in loess associated with irrigation activities and its influence on the slope stability in Heifangtai loess highland, China. *Eng. Geol.* **234**, 27–37 (2018).
19. Johansson, J. & Edeskär, T. Effects of external water-level fluctuations on slope stability. *Electron. J. Geotech. Eng.* **19**(K), 2437–2463 (2014).
20. Kellermann, P., Schöbel, A., Kundela, G. & Thieken, A. H. Estimating flood damage to railway infrastructure–the case study of the March River flood in 2006 at the Austrian Northern Railway. *Nat. Hazard.* **15**(11), 2485–2496 (2015).
21. Polemio, M. & Lollino, P. Failure of infrastructure embankments induced by flooding and seepage: A neglected source of hazard. *Nat. Hazard.* **11**(12), 3383–3396 (2011).
22. Tsubaki, R., Kawahara, Y., Sayama, T. & Fujita, I. Analysis of hydraulic and geomorphic condition causing railway embankment breach due to inundation flow. *J. Hydrosci. Hydraul. Eng* **30**, 87–99 (2012).
23. Roshan, M. J., Rashid, A. S. A. & Wahab, N. A. Stability of railway embankment in saturated and unsaturated conditions. *IOP Conf Ser Mater Sci Eng* **1153**, 012007 (2021).
24. Ahmadi, H. Analyzing the effectiveness of anti-slide piles for slope stabilization against seismic loading using discrete element method. *Eur. J. Environ. Civ. Eng.* **26**(16), 8133–8151 (2022).
25. Tuskan, Y. & Basari, E. Evaluation of sustainable slope stability with anti-slide piles using an integrated AHP-VIKOR methodology. *Sustainability* **15**(15), 12075 (2023).
26. Abd El Raouf, M. E. Improvement stability of slopes using anti-slide piles. Journal Homepage: www. feng. bu. edu. eg, **1** (42), 104–108 (2019).
27. Huang, Y., He, Z., Yashima, A., Chen, Z. & Li, C. Multi-objective optimization design of pile-anchor structures for slopes based on reliability theory considering the spatial variability of soil properties. *Comput. Geotech.* **147**, 104751 (2022).
28. Deng, D. P., Li, L. & Zhao, L. H. Stability analysis of slopes reinforced with anchor cables and optimal design of anchor cable parameters. *Eur. J. Environ. Civ. Eng.* **25**(13), 2425–2440 (2021).
29. Blanco-Fernandez, E., Castro-Fresno, D., Díaz, J. D. C. & Lopez-Quijada, L. Flexible systems anchored to the ground for slope stabilisation: Critical review of existing design methods. *Eng. Geol.* **122**(3–4), 129–145 (2011).
30. Fan, J., Zhang, Y., Yuan, K. & Zhou, W. Research on the correlation between PMT and SPT in loess silty clay. *Chin. J. Rock Mech. Eng.* **42**(S1), 3823–3831. https://doi.org/10.13722/j.cnki.jrme.2022.0648 (2023).
31. Zhou, H., Ma, F., Yu, X. & Zheng, G. Fragility assessment for the rainfall-induced embankments on silty soils. *Front. Built Environ.* **10**, 1389576 (2024).
32. Li, S., Li, Y. & Xu, L. Deformation pattern and failure mechanism of railway embankment caused by lake water fluctuation using earth observation and on-site monitoring techniques. *Water* **15**(24), 4284 (2023).
33. Hou, D., Zeng, F., Deng, J., Wei, H. & Xu, R. Failure mechanism of loess landslide induced by water stagnation on the combined surface. *Front. Earth Sci.* **12**, 1467209 (2024).
34. Zhuang, J., Kong, J., Zhu, Y. & Peng, J. The structural evolution of undisturbed loess due to water infiltration. *Sci. Rep.* **14**(1), 14880 (2024).
35. Linrong, X., Usman, A. B., Bello, A. A. D. & Yongwei, L. Rainfall-induced transportation embankment failure: A review. *Open Geosci.* **15**(1), 20220558 (2023).
36. Pezowicz, P. & Choma-Moryl, K. Moisture content impact on mechanical properties of selected cohesive soils from the wielkopolskie voivodeship southern part. *Studia Geotech. et Mech* **37**(4), 37–46 (2015).
37. Fan, J., Zhang, Y., Yuan, K. & Zhou, W. Experimental study on the bearing capacity and effective anchorage lengths of inclined steel grouting pipes in loess embankment slope. *PLoS ONE* **19**(12), e0316528 (2024).

Author contributions

Conceptualization: K. Y.; Methodology: J. F.; Formal analysis and investigation: J. F.; Writing—original draft preparation: J. F.; Writing—review and editing: J. F., Y. P., Z. X., J. C., B. L.; Funding acquisition: Y. Z.; Resources: W. Z.; Supervision: Y. Z.

Funding

The authors would give our sincere acknowledgements to the financial support from Technology Research and Development Plan of China State Railway Group Co., Ltd. under grant number N2022G020, China Academy of Railway Sciences Co., Ltd. fund program (Grant No. 2023YJ219, 2024YJ250), as well as Qinghai Province Key Research and Development and Transformation Plan under grant number 2022-SF-158.

Declarations

Competing interests

The authors declare no competing interests.

Additional information

Correspondence and requests for materials should be addressed to W.Z.